

# CHAPTER 1

---

## Moment Invariants of Vector and Tensor Fields

---

Jan Flusser, Tomáš Suk, Jitka Kostková, Matěj Lébl, and Ibrahim Ibrahim

Vector and tensor fields are multidimensional data, where in each pixel/voxel the field is assigned to a vector or a matrix. The fields describe particle velocity, optical flow, stress and conductivity tensors, and similar phenomena. One of the challenging tasks is the invariant detection of patterns of interest. Invariants to total rotation and affine transformation of the field are desirable to accomplish this task. In this chapter, we review a recent development of this research area and show several practical applications on real data.

---

Jan Flusser, Tomáš Suk, Jitka Kostková, Matěj Lébl  
Czech Academy of Sciences, Institute of Information Theory and Automation,  
Pod Vodarenskou vezi 4, 182 08 Prague 8  
Prague, Czech Republic  
e-mail: flusser,suk,kostkova,lebl@utia.cas.cz

Ibrahim Ibrahim  
MR Unit, Department of Diagnostic and Interventional Radiology,  
Institute for Clinical and Experimental Medicine IKEM, Vídeňská 1958/9, Prague 4  
Prague, Czech Republic  
e-mail: ibib@ikem.cz

## 1.1 Introduction

Vector fields and tensor fields are a special kind of multidimensional data, which are in a certain sense similar to digital images, but are distinct from them in several aspects. In each pixel/voxel, a vector or a matrix is assigned to the field. The vector shows the direction and the magnitude of the measured quantity, the matrix carries additional directional information.

Vector fields appear in numerous scientific and engineering areas, such as in mechanical engineering, fluid dynamics, medical imaging, computer vision, and meteorology. They describe particle movement, wind velocity, optical/motion flow, image gradient, and other phenomena. Vector fields may be used to represent and visualize flowing water in a pipe, an air flow around an aircraft wing or around a coachwork, and a meteorological wind velocity map (see Fig.(1.1) for an example).

Tensor fields appear for instance in diffusion tensor imaging, which is a modern MRI-based technique for an examination of tissues with internal anisotropic structure, such as neural axons of white matter in the brain and peripheral nerve fibres. In mechanical engineering, a tensor field is obtained when measuring elastic deformations and stress inside a material.

In fluid mechanics, flow fields and their mathematical models (mostly based on the Navier–Stokes equations) have been studied for centuries. However, in connection with new devices/techniques producing vector or even tensor field data, the tasks have appeared which seem to be better resolved by signal-processing approach rather than by traditional fluid mechanics techniques.

A typical example of such task is the detection of various patterns of interest. It comprises not only detection of singularities such as vortices, saddle points, vortex-saddle combinations, and double vortices (these could be found by traditional techniques as well), but also detection of arbitrary patterns, which are similar to the pattern stored in the pattern-of-interest database (these patterns may be extracted from similar fields or obtained as a result of simulations). Since the patterns of interest may not have any special mathematical properties, their detection by traditional tools is questionable or even impossible. For engineers and designers, it is very important to identify these patterns of interest in the flow, because they may increase the friction, vary the pressure, or decrease the speed of the medium, which consequently increases the power and cost necessary to transport it through the pipe or to move an object through air or water.

Pattern detection can be accomplished by *template matching*, which is a technique widely applied in image processing but relatively new in vector field analysis. The search algorithm evaluates the similarity between the template and a field patch and must be primarily *invariant* with respect to all possible pattern deformations, which might be present (for instance, the template stored in the database may depict a circular vortex, but we want to find also all elliptic vortices of arbitrary size and orientation, which may appear near obstacles and boundaries). Figure 1.2 schematically shows the pattern matching problem in a vector field.

Due to the difference between “traditional” images and vector/tensor fields, special matching methods have to be developed. In this chapter, we present an overview of methods for the description and matching of vector/tensor field patterns under

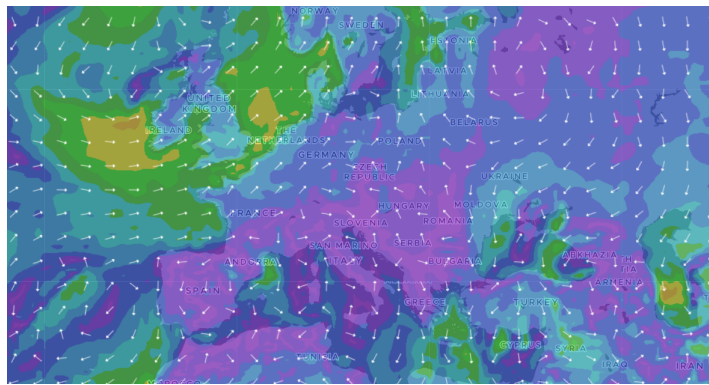


Figure 1.1: An example of 2D vector field – a wind velocity map of Europe (downloaded from [windfinder.com](http://windfinder.com)).

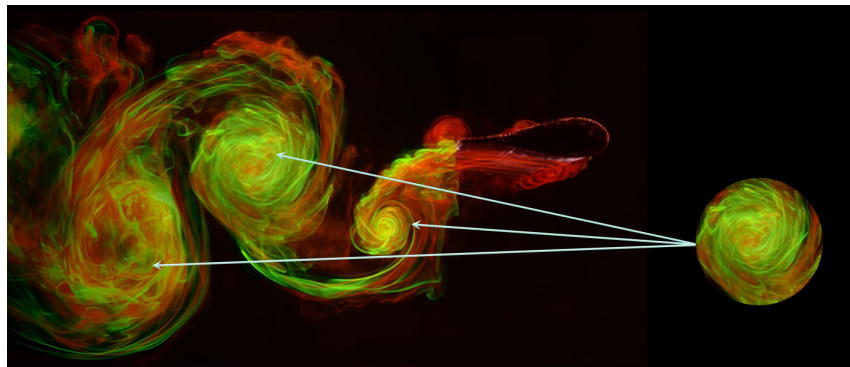


Figure 1.2: Vortex detection in a swirling fluid by template matching. The method should detect all instances of the template regardless of their position and deformation.

an unknown rotation or affine transformation of the field. Unlike digital images, the transformation of a field acts not only on the spatial coordinates but also on the field values, which makes the detection different from the image case. To measure the similarity between the template and the field patch, special invariants with respect to a *total affine transformation* must be employed. As we show, they can be designed from the field moments. Although the invariants can be generated by various methods, in this chapter we present the method of complex moments for rotation invariants of vector fields, the method of geometric primitives for affine invariants of vector fields, and the tensor method for invariants of tensor fields.

The chapter is structured as follows. After giving a survey of relevant literature in Section 1.2 and introducing the basic terms of a vector field theory in Section 1.3, we present invariants to rotation of a vector field in Section 1.4. In Section 1.5, vector field invariants w.r.t. total affine transformation are presented. Affine invariants of tensor fields are introduced in Section 1.6. At the end of each section, template matching experiments on real data are shown to illustrate the performance of the invariants.

## 1.2 Related Work

The problem of finding vector field invariants to total rotation was raised for the first time relatively recently by Schlemmer et al. [24], who adapted the scalar moment invariants proposed by Mostafa and Psaltis [1] and Flusser [8, 9] and designed invariants composed of geometric complex moments of the field. Schlemmer et al. used these invariants to detect specific patterns in a turbulent swirling jet flow. Rotation invariants from geometric complex moments have found several applications. Liu and Ribeiro [20] used them, along with a local approximation of the vector field by polynomials, to detect singularities on meteorological satellite images showing wind velocity. Basically, the same kind of rotation invariants were used by Liu and Yap [19] for the indexing and recognition of fingerprint images. A generalization to more than two dimensions using tensor contraction was proposed by Langbein and Hagen [18]. Bujack et al. [6, 5] studied the invariants of complex moments thoroughly, generalized the previous works, and showed that the invariants can be derived also by means of the field normalization approach. Yang et al. improved the numerical stability of the invariants by using orthogonal Gaussian–Hermite [36, 35] and Zernike [35] moments instead of the geometric ones. Later on, Bujack [3] introduced so-called flexible basis of the invariants to avoid moments that vanish on the given templates. In all these methods, the authors did not go beyond a simple total rotation/scaling template deformation, which is insufficient in many applications.

Affine invariants of 2D vector fields were firstly proposed by Kostková et al. in [16], who later presented a theory of invariants and multi-layer graphs [17]. Their theory was inspired by classical work on affine moment invariants of scalar and color images [22, 23, 10, 27, 13, 21, 12]. Generalization to vector fields of more than two dimensions and to tensor fields was theoretically proposed by Langbein and Hagen [18] and Bujack et al. [4].

## 1.3 Vector Fields and Their Transformations

In this section, we formally define a vector field, introduce the notion of its *total transformation* and show how the transformations of “traditional” images and vector fields differ from one another, even if both can be understood as particular cases of total transformations.

**Definition 1.** Let  $\mathbf{x} = (x_1, \dots, x_m)$ . An  $n$ -D vector field  $\mathbf{f}(\mathbf{x})$  is an ordered  $n$ -tuple of scalar fields  $\mathbf{f}(\mathbf{x}) = (f_1(\mathbf{x}), f_2(\mathbf{x}), \dots, f_n(\mathbf{x}))$ .

At each point  $\mathbf{x}$ , the value of  $\mathbf{f}(\mathbf{x})$  shows the measured vector. The scalar field  $f_i(\mathbf{x})$  can be understood as a graylevel image, which may contain also negative values. In this chapter, we consider only the case  $m = n = 2$  since it is the most common in practice.

By a total transformation we understand any transformation of the vector field, which acts simultaneously in spatial and function domains. Even if this definition can be used for arbitrary (non-linear) transformations, we consider only linear ones.

**Definition 2.** Let  $A$  and  $B$  be regular matrices and  $\mathbf{f}$  be a vector field. The transformation  $\mathbf{f} \rightarrow \mathbf{f}'$ , where

$$\mathbf{f}'(\mathbf{x}) = B\mathbf{f}(A^{-1}\mathbf{x}) \quad (1.1)$$

is called *total affine transformation* (TAFT) of the field  $\mathbf{f}$ . Matrix  $A$  is called *inner* transformation matrix, while matrix  $B$  is called *outer* transformation matrix.

In reality, the transformation in Eq.(1.1) is often physically constrained such that  $A = B$ . Such a model captures one of the basic properties of vector fields – if the field is transformed in the space domain, the function domain (i.e. the vector values) is transformed by the same transformation. This can be understood intuitively. Let us imagine the vector field as an array of arrows. If we deform spatially the array, the absolute orientation and length of the arrows must be changed accordingly such that their relative orientation and length is preserved (see Fig.(1.3) for an example). If  $A = B = R_\alpha$ , where  $R_\alpha$  is a rotation matrix, we speak about *total rotation*.

## 1.4 Invariants to Total Rotation of Vector Fields

Let us consider a total rotation of a vector field  $\mathbf{f}$

$$\mathbf{f}'(\mathbf{x}) = R_\alpha \mathbf{f}(R_{-\alpha} \mathbf{x}), \quad (1.2)$$

where

$$R_\alpha = \begin{pmatrix} \cos \alpha & -\sin \alpha \\ \sin \alpha & \cos \alpha \end{pmatrix}$$

is a matrix of rotation by angle  $\alpha$ .

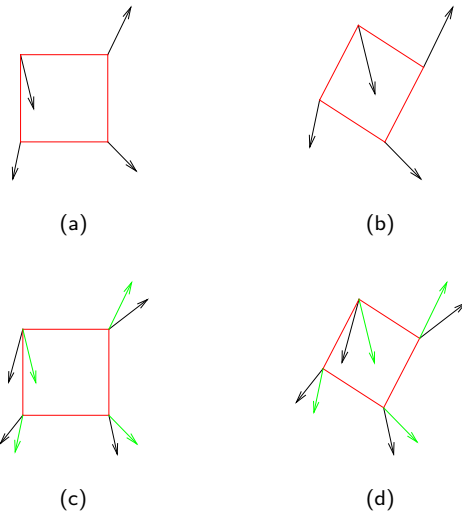


Figure 1.3: Vector field transformations: (a) an original vector field, (b) its inner affine transformation, (c) its outer affine transformation, (d) its total affine transformation. The green arrows in (c) and (d) show the vector field without the outer transformation.

### 1.4.1 Rotation Invariants From Geometric Moments

A 2D vector field can be treated as a complex-valued function

$$\mathbf{f}(x, y) = f_1(x, y) + i f_2(x, y), \quad (1.3)$$

which allows us to use a standard definition of moments. Already in the theory of moments of scalar images, it was shown [8] that the rotation invariants can be easily constructed by using *complex moments*

$$c_{pq} = \int_{-\infty}^{\infty} \int_{-\infty}^{\infty} (x + iy)^p (x - iy)^q f(x, y) dx dy, \quad (1.4)$$

which are in fact linear combinations of geometric moments

$$m_{pq} = \int_{-\infty}^{\infty} \int_{-\infty}^{\infty} x^p y^q f(x, y) dx dy. \quad (1.5)$$

Here,  $f(x, y)$  is scalar image. The scalar complex moments change under the inner rotation by angle  $\alpha$  simply as

$$c'_{pq} = e^{-i(p-q)\alpha} c_{pq} \quad (1.6)$$

(see [8] for the proof). Under a total rotation of a vector field,  $c_{pq}^{(\mathbf{f})} = c_{pq}^{(f_1)} + i c_{pq}^{(f_2)}$  fulfills

$$c_{pq}^{(\mathbf{f}') \prime} = e^{-i\alpha} e^{-i(p-q)\alpha} \cdot c_{pq}^{(\mathbf{f})} = e^{-i(p-q+1)\alpha} \cdot c_{pq}^{(\mathbf{f})}. \quad (1.7)$$

Now we can cancel the rotation parameter  $\alpha$  by multiplication of any proper powers of the  $c_{pq}$ 's. Let  $\ell \geq 1$  and further let  $k_i, p_i$ , and  $q_i$  ( $i = 1, \dots, \ell$ ) be non-negative integers such that

$$\sum_{i=1}^{\ell} k_i(p_i - q_i + 1) = 0.$$

Then

$$I = \prod_{i=1}^{\ell} c_{p_i q_i}^{k_i} \quad (1.8)$$

is invariant with respect to total rotation of a vector field.

### 1.4.2 Rotation Invariants From Gaussian–Hermite Moments

The monomials  $(x + iy)^p(x - iy)^q$ , when implemented numerically, lead to overflow and, consequently, to unstable behavior of the moments. This is why Yang et al. [35] proposed to design vector field invariants from orthogonal (OG) moments. They used moments w.r.t. Gaussian–Hermite (GH) polynomials and Zernike polynomials.

1D Gaussian–Hermite polynomials are defined as

$$H_n(x, \sigma) = H_n(x/\sigma) e^{-\frac{x^2}{2\sigma^2}}, \quad (1.9)$$

where  $H_n(x)$  is the Hermite polynomial of the  $n$ -th degree

$$H_n(x) = (-1)^n e^{x^2} \frac{d^n}{dx^n} e^{-x^2}. \quad (1.10)$$

Hermite polynomials are orthogonal on  $(-\infty, \infty)$  with the weight  $w(x) = e^{-x^2}$ . For numerical calculations, Hermite polynomials can be evaluated in a fast and stable way by means of the three-term recurrence relation

$$H_n(x) = 2xH_{n-1}(x) - 2(n-1)H_{n-2}(x) \quad (1.11)$$

with the initialization  $H_0(x) = 1$  and  $H_1(x) = 2x$ , which makes them convenient for implementation.

2D Hermite polynomials are obtained as a product

$$H_{nm}(x, y) = H_n(x)H_m(y). \quad (1.12)$$

Under coordinate rotation, they are transformed exactly in the same way as the monomials  $x^n y^m$  [32, 37] (they are actually the only separable OG polynomials with this property [33]). Thanks to this, Hermite polynomials form a convenient basis for a construction of rotation invariants of scalar images [34] and can be easily used to design vector field invariants analogous to Eq.(1.8) but numerically more stable (see [35] for a detailed derivation).

### 1.4.3 Rotation Invariants From Zernike Moments

Zernike polynomials are intrinsically 2D polynomials, which were originally proposed to describe the diffracted wavefront in phase contrast imaging [38] and have found numerous applications in mathematics, optics, and imaging. Zernike moments (ZMs) [28] have become very popular in image analysis. Their main advantage comes from the fact that they are orthogonal on a unit disk, they keep their magnitude constant under an image rotation, and their phase change is simple and easy to eliminate. The latter property ensures a straightforward construction of rotation invariants of scalar images [29].

Zernike moment of order  $n$  with repetition  $\ell$  of vector field  $\mathbf{f}$  is defined as

$$A_{n\ell} = \frac{n+1}{\pi} \int_0^{2\pi} \int_0^1 V_{n\ell}^*(r, \theta) \mathbf{f}(r, \theta) r dr d\theta, \quad (1.13)$$

where  $n = 0, 1, 2, \dots$ ,  $\ell = -n, -n+2, \dots, n$ , and  $V_{n\ell}(r, \theta)$  is the respective Zernike polynomial (see for instance [11] for its complete definition).

Under a total rotation of the field by  $\alpha$ , ZMs are transformed as

$$A'_{n\ell} = A_{n\ell} e^{-i(\ell-1)\alpha}. \quad (1.14)$$

The rotation invariants of vector fields are then obtained by phase cancellation as

$$Z_{n\ell} = A_{n\ell} (A_{n_0\ell_0})^{-(\ell-1)/(\ell_0-1)}, \quad (1.15)$$

where the normalizer should be chosen such that  $\ell_0 \neq 1$  and  $A_{n_0\ell_0} \neq 0$ . If we choose  $\ell_0 = 0$  or  $\ell_0 = 2$ , we avoid the complex roots and end up with simpler invariants

$$Z_{n\ell} = A_{n\ell} (A_{n_0\ell_0})^{\pm(\ell-1)}. \quad (1.16)$$

Similarly to the GH moments, also the Zernike moments can be efficiently computed by means of recurrent relations [11].

### 1.4.4 Experiment

The following template matching experiment illustrates the use of the GH invariants of vector fields. As the test vector field, we used the gradient of the picture of hair (see Fig.(1.4) for the original image). We chose this particular photograph to make the matching challenging. On the one hand, the picture is rich in edges so there are no large regions of a constant gradient; on the other hand there are many patches similar to each other, which makes the matching non-trivial.

We randomly selected 9 circular templates of the gradient field, rotated them by  $5^\circ$ , and matched them against the original field. The matching was carried out by searching for the minimum  $\ell_2$ -distance in the space of the GH invariants of orders  $p + q \leq 4$  between the template and all field patches of the same size. Eight templates were found in their exact location, one was matched with a localization error of 1 pixel (see Fig.(1.5a)). We repeated this experiment with template rotations  $23^\circ$ ,  $41^\circ$ ,  $59^\circ$ , and  $77^\circ$ , respectively. The results were always exactly the same as depicted in Fig.(1.5a)



Figure 1.4: The original picture of hair.

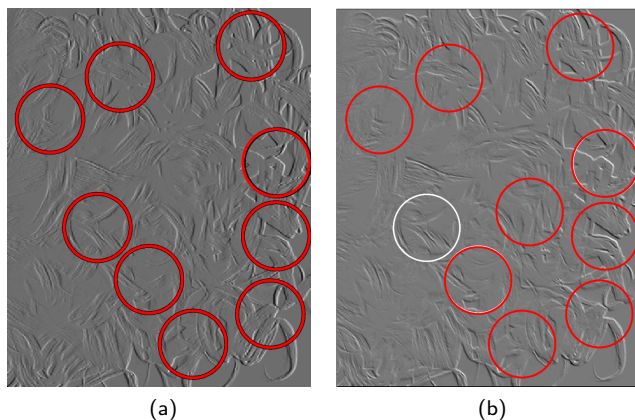


Figure 1.5: Gradient field of the hair picture (only the magnitudes are displayed). (a) Ground-truth template positions and the positions localized by the GH invariants (red). The ground-truth and the localized positions coincide. (b) The results when only the field magnitudes and scalar GH invariants were used. Eight templates were localized correctly, but one (white) was totally mismatched.

(including that single one-pixel error). We can conclude that the performance of the GH invariants in template matching is very good, regardless of the actual template content and of the template rotation.

To illustrate that the vector field template matching cannot be reduced to scalar image matching, we repeated this experiment on the field magnitudes only. The field magnitudes form a traditional scalar graylevel image. We used the same matching algorithm as before but with scalar GH invariants [34] instead of the vector field invariants. On the same set of the templates, eight of them were localized correctly, but one was mismatched with a different area of the image (see Fig.(1.5b)). We achieved the same results regardless of the template orientations and similar results have been achieved for other settings. This demonstrates that both orientation and magnitude of the vector field should be used together, and the task cannot be restricted to the traditional scalar image matching.

## 1.5 Affine Invariants of Vector Fields

In this section, we describe vector field moment invariants w.r.t. total affine transformation (VFAMIs). This theory was originally proposed in [17]. We first show how to design invariants w.r.t. the inner transformation, then we consider solely the outer transformation, and finally we combined both together to obtain invariants w.r.t. the total affine transformation of the field.

### 1.5.1 Invariants to Inner Transformation

Let us first construct the VFAMIs for the particular case of the transformation Eq.(1.1), where  $B = I$  (this is essentially the problem of AMIs for two-band images). We start by constructing the AMIs for components  $f_1$  and  $f_2$  separately. To do so, we use the method proposed in [25] and further elaborated in [27], which guarantees to produce a complete set.

Let us consider two arbitrary points  $\mathbf{x}_1 = (x_1, y_1)$ ,  $\mathbf{x}_2 = (x_2, y_2)$  from the support of  $\mathbf{f}$ . Let us denote the “cross-product” of these points as  $C_{12}$ :

$$C_{12} = x_1 y_2 - x_2 y_1 .$$

Geometric meaning of  $C_{12}$  is the oriented double area of the triangle, whose vertices are  $(x_1, y_1)$ ,  $(x_2, y_2)$ , and  $(0, 0)$ . After an affine transformation  $\mathbf{x}' = A\mathbf{x}$  has been applied, the cross-product is transformed as  $C'_{12} = J_A \cdot C_{12}$ , where  $J_A = \det(A)$  is the Jacobian of the transformation. This proves that  $C_{12}$  is a relative invariant with respect to inner transformation  $A$ . Now we consider various numbers of points  $(x_i, y_i)$  and we integrate their cross-products (or some integer powers of their cross-products) over the support of  $\mathbf{f}$ . These integrals can be expressed in terms of moments and, after eliminating the Jacobian by a proper normalization, they yield absolute affine invariants.

More precisely, having  $r > 1$  distinct points  $(x_1, y_1), \dots, (x_r, y_r)$ , we define functional  $I$  of scalar  $f$  depending on  $r$  and on non-negative integers  $n_{kj}$  as

$$I(f) = \int_{-\infty}^{\infty} \cdots \int_{-\infty}^{\infty} \prod_{k,j=1}^r C_{kj}^{n_{kj}} \cdot \prod_{i=1}^r f(x_i, y_i) dx_i dy_i. \quad (1.17)$$

Note that it is meaningful to consider only  $j > k$ , because  $C_{kj} = -C_{jk}$  and  $C_{kk} = 0$ .

After an inner affine transformation we have  $f'(\mathbf{x}) = f(A^{-1}\mathbf{x})$  and  $I(f')$  becomes

$$\begin{aligned} I(f') &= \int_{-\infty}^{\infty} \cdots \int_{-\infty}^{\infty} \prod_{k,j=1}^r C_{kj}^{n_{kj}} \cdot \prod_{i=1}^r f(A^{-1}\mathbf{x}_i) dx_i dy_i \\ &= \int_{-\infty}^{\infty} \cdots \int_{-\infty}^{\infty} \prod_{k,j=1}^r (C_{kj}^{n_{kj}})' \cdot \prod_{i=1}^r f(x_i, y_i) |J_A|^r dx_i dy_i \\ &= J_A^w |J_A|^r \cdot I(f), \end{aligned} \quad (1.18)$$

where  $w = \sum_{k,j} n_{kj}$  is the *weight* of the invariant and  $r$  is its *degree*. Hence,  $I(f)$  is a relative affine invariant. If  $I(f)$  is normalized by  $m_{00}^{w+r}$ , we obtain a desirable absolute affine invariant

$$\left( \frac{I(f)}{m_{00}^{w+r}} \right)' = \left( \frac{I(f)}{m_{00}^{w+r}} \right) \quad (1.19)$$

(if  $w$  is odd and  $J < 0$ , the sign change occurs in Eq.(1.19)). If we expand the integrand in Eq.(1.17) and integrate term-wise, we obtain an expression of  $I$  in terms of geometric moments of  $f$ . Varying  $r$  and  $n_{kj}$ , we can generate infinitely many invariants of all orders. Such a set is complete but highly redundant. The process of eliminating reducible invariants is described in [27].

The invariants from Eq.(1.19) can be derived separately for both field components  $f_1$  and  $f_2$ . In addition to that, we can further employ the fact that the transformation  $A$  is the same for both components, which brings a possibility of constructing *joint invariants* (i.e. invariants containing the moments of both  $f_1$  and  $f_2$ ). This idea was proposed in [26] in the context of invariants for color images and slightly increases the number of independent invariants.

## 1.5.2 Invariants to Outer Transformation

Now let us consider an arbitrary regular  $B$  in the transformation Eq.(1.1), but assume for simplicity that  $A = I$ , so only an outer transformation of the vector field is effective. We proceed analogously to the previous section. The role of  $C_{kj}$  has been taken over by “component cross-products”  $F_{kj}$

$$F_{kj} = f_1(x_k, y_k) f_2(x_j, y_j) - f_1(x_j, y_j) f_2(x_k, y_k).$$

$F_{kj}$  is a relative invariant w.r.t. outer affine transformation as

$$F'_{kj} = J_B \cdot F_{kj},$$

where  $J_B = \det(B)$ . The simplest moment invariants are given as

$$O_{pqst}(\mathbf{f}) = \int_{-\infty}^{\infty} \cdots \int_{-\infty}^{\infty} x_1^p y_1^q x_2^s y_2^t F_{12} dx_1 dx_2 dy_1 dy_2, \quad (1.20)$$

which yields, after the term-wise integration, the moment form

$$O_{pqst}(\mathbf{f}) = m_{pq}^{(1)} m_{st}^{(2)} - m_{st}^{(1)} m_{pq}^{(2)}, \quad (1.21)$$

where

$$m_{pq}^{(i)} = \int_{-\infty}^{\infty} \int_{-\infty}^{\infty} x^p y^q f_i(x, y) dx dy. \quad (1.22)$$

The relative invariance of  $O_{pqst}(\mathbf{f}') = J_B \cdot O_{pqst}(\mathbf{f})$  follows immediately from the invariance of  $F_{12}$ . Eq.(1.21) yields a non-trivial invariant for arbitrary combinations of indices except  $(p, q) = (s, t)$  (note that  $O_{pqpq}(\mathbf{f}) = 0$  for any  $p, q$ , and  $\mathbf{f}$ ). Swapping of the indices  $(p, q) \leftrightarrow (s, t)$  just changes the sign as  $O_{pqst}(\mathbf{f}) = -O_{stpq}(\mathbf{f})$  and does not yield an independent invariant. Hence, using all non-trivial configurations of indices  $p, q, s, t$  up to the given order  $R$ , we obtain  $R(R+1)(R+2)(R+3)/8$  invariants of the form Eq.(1.21). They form a complete system, because we can recover all moments of the field from its invariants, up to the four degrees of freedom due to the transformation matrix  $B$  (see [17] for the proof). The above invariants are, however, not independent, because there exist only  $(R+1)(R+2)$  moments.

Invariants to outer transformation of a field can also be obtained in a general form analogous to Eq.(1.17) as

$$O(\mathbf{f}) = \int_{-\infty}^{\infty} \cdots \int_{-\infty}^{\infty} \prod_{k,j=1}^r F_{kj}^{v_{kj}} \cdot \prod_{i=1}^r x_i^{p_i} y_i^{q_i} dx_i dy_i, \quad (1.23)$$

which leads to relative invariants given by

$$O(\mathbf{f}') = J_B^v \cdot O(\mathbf{f}),$$

where  $v = \sum v_{kj}$ . The invariants of the form Eq.(1.21) are just particular cases of this general expression.

### 1.5.3 Invariants to Total Transformation

In this section, we go to the core of the problem. We show how to put the inner and outer invariants together and we propose vector field invariants w.r.t. total affine transformation. The key definition, analogous to Eq.(1.17) and Eq.(1.23), is now

$$V(\mathbf{f}) = \int_{-\infty}^{\infty} \cdots \int_{-\infty}^{\infty} \prod_{k,j=1}^r C_{kj}^{n_{kj}} \cdot F_{kj}^{v_{kj}} \cdot \prod_{i=1}^r dx_i dy_i. \quad (1.24)$$

$V(\mathbf{f})$  is a relative invariant as

$$V(\mathbf{f}') = J_B^v J_A^w |J_A|^r V(\mathbf{f}). \quad (1.25)$$

To eliminate  $J_A$  and  $J_B$  and obtain an absolute invariant, we have to normalize the relative invariant Eq.(1.24) by proper powers of other two relative invariants such that both Jacobians get canceled.

If used extensively with many various parameters, Eq.(1.24) yields a huge number of redundant invariants. The first step to eliminate the redundancy is to fulfill the constraint that  $V(\mathbf{f})$  must be composed solely of moments of the field  $\mathbf{f}$  (and not of the moments of higher powers of  $\mathbf{f}$ ). This is equivalent to the constraints imposed on the powers  $v_{kj}$ . Considering all possible index pairs  $(k, j)$ , each of the points  $(x_1, y_1), \dots, (x_r, y_r)$  must be involved just once in all  $F_{kj}$ 's used. Hence, any  $v_{kj}$  can only equal 0 or 1,  $v = r/2$  (which immediately implies that  $r$  must be even), and  $v_{kj} = 0$  for all  $k \geq j$  (this constraint is because  $F_{kj} = -F_{jk}$  and  $F_{kk} = 0$ , so it would be useless to include them into the invariant). If  $v_{kj} = 1$ , then  $v_{mj} = v_{jm} = v_{km} = v_{mk} = 0$  for all index pairs different from  $(k, j)$ .

We may notice, that generating VFAMIs from Eq.(1.24), even if the choice of  $v_{kj}$  has been constrained as mentioned above, leads to many invariants, which are identically zero or which are somehow dependent on the other invariants that have been obtained from Eq.(1.24), with other settings of the parameters. Dependent invariants do not contribute to the recognition power of the system and only increase the dimensionality of the invariant set. It is highly desirable to identify them and exclude them from the set. An algorithm for detection of dependent invariants is proposed in [17]. It is based on representation of the invariants by *multi-layer graphs* and on sequential search of the graph space.

As an example, we show four simple VFAMIs in explicit forms below; hundreds of other invariants generated from Eq.(1.24) can be found on our webpage [zoi.utia.cz/affine-vector-fields](http://zoi.utia.cz/affine-vector-fields).

The simplest non-trivial choice is  $r = 2$  and  $n_{12} = v_{12} = 1$ , which yields

$$V_a = m_{10}^{(1)} m_{01}^{(2)} - m_{10}^{(2)} m_{01}^{(1)}.$$

The choice of  $r = 2, v_{12} = 1$  and  $n_{12} = 3$  yields

$$V_b = m_{30}^{(1)} m_{03}^{(2)} - 3m_{21}^{(1)} m_{12}^{(2)} + 3m_{12}^{(1)} m_{21}^{(2)} - m_{03}^{(1)} m_{30}^{(2)}.$$

The parameters  $r = 2, v_{12} = 1$  and  $n_{12} = 5$  lead to the invariant

$$V_c = m_{50}^{(1)} m_{05}^{(2)} - 5m_{41}^{(1)} m_{14}^{(2)} + 10m_{32}^{(1)} m_{23}^{(2)} - 10m_{23}^{(1)} m_{32}^{(2)} + 5m_{14}^{(1)} m_{41}^{(2)} - m_{05}^{(1)} m_{50}^{(2)}.$$

If we choose  $r = 4, v_{12} = v_{34} = 1$  and  $n_{12} = n_{13} = n_{24} = n_{34} = 1$ ,  $n_{kj} = 0$  otherwise, we obtain

$$\begin{aligned} V_d = & - \left( m_{20}^{(1)} \right)^2 \left( m_{02}^{(2)} \right)^2 + 4m_{20}^{(1)} m_{11}^{(1)} m_{11}^{(2)} m_{02}^{(2)} + 2m_{20}^{(1)} m_{02}^{(1)} m_{20}^{(2)} m_{02}^{(2)} \\ & - 4m_{20}^{(1)} m_{02}^{(1)} \left( m_{11}^{(2)} \right)^2 - 4 \left( m_{11}^{(1)} \right)^2 m_{20}^{(2)} m_{02}^{(2)} + 4m_{11}^{(1)} m_{02}^{(1)} m_{20}^{(2)} m_{11}^{(2)} \\ & - \left( m_{02}^{(1)} \right)^2 \left( m_{20}^{(2)} \right)^2 \end{aligned}$$

### 1.5.4 Invariants to Special Total Transformation

The inner and outer transformations of a vector field are often the same, i.e.  $A = B$  and Eq.(1.25) is simplified to the form

$$V(\mathbf{f}') = J_A^{w+r/2} |J_A|^r V(\mathbf{f}). \quad (1.26)$$

The normalization can be accomplished just by one invariant, while the other one, which was needed to cancel  $J_B$  before, can be saved for recognition. This is, however, not the only difference. Since the number of degrees of freedom of the transformation has been reduced from eight to four, one may expect the existence of four additional independent invariants.

For a special total transformation, there exists yet another possibility how to generate invariants. We can replace the “intensity cross-product”  $F_{kj}$  by the “mixed cross-product”

$$D_{kj} = y_j f_1(x_k, y_k) - x_j f_2(x_k, y_k).$$

$D_{kj}$  is a relative invariant w.r.t. special total transformation as

$$D'_{kj} = J_A \cdot D_{kj}.$$

Unlike the previous case, here generally  $D_{kj}$  and  $D_{jk}$  are independent, and  $D_{kk} \neq 0$ . Similarly to Eq.(1.24), we define functional

$$W(\mathbf{f}) = \int_{-\infty}^{\infty} \cdots \int_{-\infty}^{\infty} \prod_{k,j=1}^r C_{kj}^{n_{kj}} \cdot D_{kj}^{u_{kj}} \cdot \prod_{i=1}^r dx_i dy_i, \quad (1.27)$$

which is a relative invariant because

$$W(\mathbf{f}') = J_A^{w+u} |J_A|^r W(\mathbf{f}). \quad (1.28)$$

Equation (1.27) leads to moments only under certain restrictions, imposed on exponents  $u_{kj}$ . Each of the points  $(x_1, y_1), \dots, (x_r, y_r)$  must be involved just once as a field argument in all  $D_{kj}$ 's used. Hence, any  $u_{kj}$  can only equal 0 or 1 and  $u \equiv \sum u_{kj} = r$ .

We may go even further and generate invariants of the form

$$Z(\mathbf{f}) = \int_{-\infty}^{\infty} \cdots \int_{-\infty}^{\infty} \prod_{k,j=1}^r C_{kj}^{n_{kj}} \cdot F_{kj}^{v_{kj}} \cdot D_{kj}^{u_{kj}} \cdot \prod_{i=1}^r dx_i dy_i. \quad (1.29)$$

In this case, however, the constraints on  $v$  and  $u$  are different from the previous cases and are linked together. It still holds that each point  $(x_i, y_i)$  must appear just once as a field argument in the integrand. Hence,  $2v + u = r$ . Any  $v_{kj}$  and  $u_{kj}$  can only equal 0 or 1 as before, but they are further constrained as follows. If  $v_{kj} = 1$ , then  $v_{mj} = v_{jm} = v_{km} = v_{mk} = 0$  for all index pairs except  $(k, j)$  and  $u_{km} = u_{jm} = 0$  for any  $m$ . If  $u_{kj} = 1$ , then  $u_{km} = 0$  for any  $m \neq j$  and  $v_{km} = v_{mk} = 0$  for any  $m$ .

$Z$  is again a relative invariant, since

$$Z(\mathbf{f}') = J_A^{w+v+u} |J_A|^r Z(\mathbf{f}). \quad (1.30)$$

It should be, however, noted that each of the sets generated by Eqs.(1.24), (1.27), and (1.29) is highly redundant even on its own, and this redundancy increases, if two or all three sets are used together. Actually, the invariants obtained from Eq.(1.24), and Eq.(1.27) are nothing but a subset of those obtained from Eq.(1.29). A careful selection of independent (or at least irreducible) invariants is highly recommended for practical applications.

## 1.5.5 Experiments

### 1.5.5.1 Template matching in a fluid flow field

In this experiment, we demonstrate the applicability of the proposed invariants in an important problem from fluid dynamics engineering – vortex detection in a fluid flow vector field. We used the field showing the Kármán vortex street, which is a repeating pattern of swirling vortices caused by the flow of a fluid around blunt bodies. In the Kármán pattern, we can see several vortices arranged into two rows. The orientation of the “street” is given by the main flow direction and is generally not known a priori. The data used in this experiment come from a computer simulation, not from a real physical measurement. The simulation resulted in a 300-frame video, showing the time-development of the Kármán street.

In the initial frame, we selected a template with a typical vortex, see Fig.(1.6). Then we deformed the video by two different TAFTs, which comprised anisotropic scaling with a factor of  $5/4$  and  $7/4$ , respectively. The task is to find all vortices of a similar shape modulo TAFT in each frame of the deformed video. The search is performed in the space of invariants  $Z_i$ . We search for all local minima of  $\ell_2$ -distance below a user-defined threshold. Such a task definition is rather “soft”, because it specifies neither the significance of the vortices to be detected nor the required degree of similarity with the template. The results may be controlled by the number/order of the invariants we use and also by the choice of the threshold.

We matched the template to each frame individually. We repeated the experiment for various maximum invariant order. So, we matched the templates in ten videos, which means we processed 3000 frames altogether. The resulting videos showing the vortex tracking can be found at [zoi.utia.cas.cz/Experiment-with-Karman-Street](http://zoi.utia.cas.cz/Experiment-with-Karman-Street). Two sample frames, one for each deformation, can be seen in Fig.(1.7).

Since the ground truth is not known in this experiment, the matching accuracy cannot be evaluated quantitatively. However, visual inspection of the videos provide a good insight into the performance of the method. Most of the vortices were correctly found, but we can also observe some gross errors. They arose most probably because the neighborhood, the invariants were calculated from, was always circular and of the same size as the original template.

### 1.5.5.2 Vortex detection in NOAA data

In this experiment, we show on real data how our method can be used for vortex detection in weather satellite images. We used the world wind maps from the NOAA

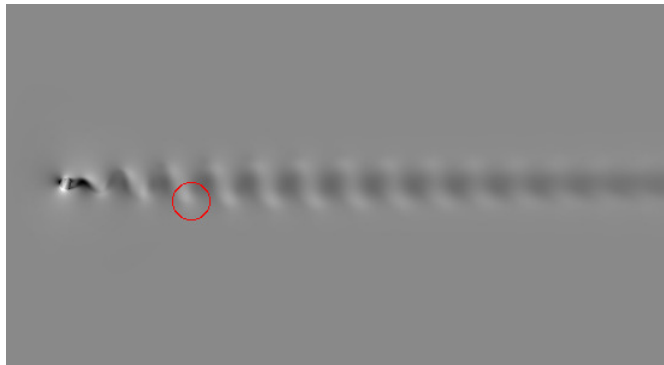
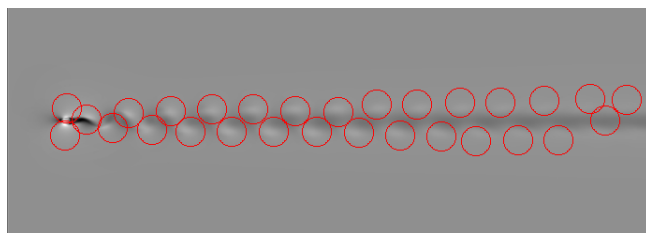
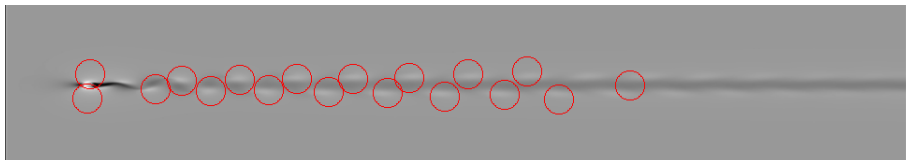


Figure 1.6: The Kármán vortex street with the selected template (the first frame of the video).



(a)



(b)

Figure 1.7: The detected vortices in the deformed field when invariants  $Z_i$  up to 7th order were employed. The deformation comprised anisotropic scaling with factors  $5/4$  (top) and  $7/4$  (bottom). The full videos can be found at [zoi.utia.cas.cz/Experiment-with-Karman-Street](http://zoi.utia.cas.cz/Experiment-with-Karman-Street).

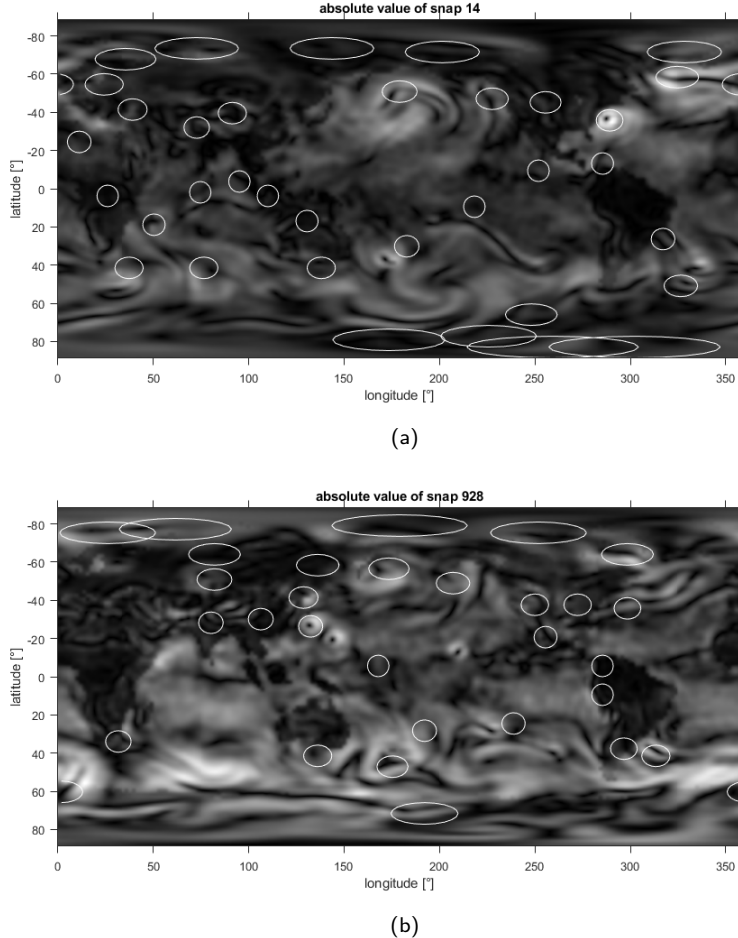


Figure 1.8: Vortex detection in two NOAA images by means of the invariants. The images display the wind magnitude only but the orientation is available as well and was used for the detection.

satellite [14], which are publicly available through [www.esrl.noaa.gov/psd/](http://www.esrl.noaa.gov/psd/). We used 18 frames from different days. We extracted three typical circular templates of a wind vortex of the same size (two from the northern and one from the southern hemisphere). Then we tried to locate vortices of the same shape in the other frames. The results achieved by the invariants in two sample frames are shown in Fig.(1.8). For the template matching, we used 28 independent invariants up to the order six (both types  $V_i$  and  $Z_i$  were included). Since there is no measurable ground truth, we are left to a visual evaluation. We can see the detection works quite well. Thanks to the affine invariance, also some vortices that exhibit an elongated shape due to data resampling in polar areas were detected (when searching the polar areas, the templates were not resampled, only the underlaying patch in the image was taken elliptical rather than circular). The method missed some vortices which look similar to the templates in magnitudes but their structure is different.

## 1.6 Affine Invariants of Tensor Fields

### 1.6.1 Introduction to tensors

Tensor fields can be understood as a generalization of vector fields, where in each pixel a matrix is stored. Tensors are used in description of anisotropic material properties, in elasticity/deformation measurement, and in conductivity mapping.

Intuitively speaking, a tensor is an array of numbers and the rank of a tensor determines the dimensionality of this array. Special cases include scalars, which are tensors of rank zero, vectors, which are tensors of rank one, and matrices, which are tensors of rank two. The tensors have two types of indices, *contravariant* and *covariant*. They differ from each other in behavior under an affine transformation of the space.

The dimensionality and the rank of tensor fields used in practice is limited. The most common tensor fields in physics are Cauchy stress tensor, viscous stress tensor, diffusion tensor, and Maxwell stress tensor. All of them have dimension three and contravariant rank two, i.e. they look like a  $3 \times 3$  matrix in each voxel. The Cauchy stress tensor describes an internal stress at a point inside a solid material. It is symmetric, i.e.  $\sigma^{ij} = \sigma^{ji}$ , so, it contains only six independent parameters. The diagonal elements express magnitude and direction, while the off-diagonal elements express the transverse components of the inner stress.

### 1.6.2 Covariant and contravariant indices

The difference between the covariant and contravariant indices manifests itself under spatial transformations. The tensor is multiplied by the matrix of the direct transformation on behalf of each covariant index and by the matrix of the inverse transformation on behalf of each contravariant index. The covariant indices are notated as subscripts, e.g.  $\nu_{ij}$ , the contravariant indices are notated as superscripts, e.g.  $\nu^{ij}$ . The number of covariant indices is called *covariant rank* of the tensor, the number of contravariant indices is called *contravariant rank*. The sum of both ranks gives the total rank of the tensor.

The range of indices equals the dimension of the space, i.e.  $i = 1, 2$  in 2D and  $i = 1, 2, 3$  in 3D. Let  $\mathbf{A}$  be a matrix representing an affine transformation. A tensor of covariant rank two behaves under this transformation as

$$\boldsymbol{\nu}'_{ij} = \sum_{k=1}^d \sum_{\ell=1}^d \mathbf{A}_i^k \mathbf{A}_j^\ell \boldsymbol{\nu}_{k\ell}, \quad (1.31)$$

where  $d$  is the dimension of the space. Similarly, for a tensor of contravariant rank two, we have

$$\boldsymbol{\nu}'^{ij} = \sum_{k=1}^d \sum_{\ell=1}^d (\mathbf{A}^{-1})_k^i (\mathbf{A}^{-1})_\ell^j \boldsymbol{\nu}^{k\ell}. \quad (1.32)$$

We may have even a tensor with both covariant and contravariant indices, which behaves as

$$\boldsymbol{\nu}'^j_i = \sum_{k=1}^d \sum_{\ell=1}^d \mathbf{A}_i^k (\mathbf{A}^{-1})_\ell^j \boldsymbol{\nu}_k^\ell. \quad (1.33)$$

### 1.6.3 Basic Operations With Tensors

Tensor multiplication is defined as

$$\boldsymbol{\sigma}_p^{ijkl} = \boldsymbol{\sigma}_1^{ij} \boldsymbol{\sigma}_2^{kl}, \quad i, j, k, \ell = 1, \dots, 3, \quad (1.34)$$

where  $\boldsymbol{\sigma}_p \in \mathbb{R}^{3 \times 3 \times 3 \times 3}$ , i.e. each component of the first tensor is multiplied by each component of the second tensor. The tensor product is noted as

$$\boldsymbol{\sigma}_p = \boldsymbol{\sigma}_1 \otimes \boldsymbol{\sigma}_2. \quad (1.35)$$

Addition of two Cauchy stress tensors is defined as

$$\boldsymbol{\sigma}_s^{ij} = \boldsymbol{\sigma}_1^{ij} + \boldsymbol{\sigma}_2^{ij}, \quad i, j = 1, \dots, 3, \quad (1.36)$$

i.e. only the corresponding components are added. The result  $\boldsymbol{\sigma}_s = \boldsymbol{\sigma}_1 + \boldsymbol{\sigma}_2$  is again a Cauchy stress tensor.

The viscous stress tensor is an analogy of the Cauchy stress tensor in fluids. It may have antisymmetric component. The Maxwell stress tensor is an analogy of the Cauchy stress tensor for electromagnetic forces. In this paper, we work with the diffusion tensor  $\mathbf{D} \in \mathbb{R}^{3 \times 3}$ . It is a second-rank three-dimensional symmetric tensor similar to the Cauchy stress tensor.

### 1.6.4 Tensor Contraction

Tensor contraction is an important operation in tensor algebra. It is the sum over two indices, one covariant and one contravariant. Let us consider a tensor  $\boldsymbol{\nu}_i^j$ . Its contraction equals

$$c = \sum_{i=1}^d \nu_i^i. \quad (1.37)$$

In the case of a second-rank tensor (matrix), the contraction is equivalent to the trace of the matrix. In so-called Einstein notation, the symbol of sum is omitted and we write just  $c = \nu_i^i$ . The contraction is sometimes denoted as

$$c = \sum_{(i,j)} \nu_i^j, \quad (1.38)$$

which means the summation goes over those components of  $\nu_i^j$ , where  $i = j$ .

If we observe the contraction of  $\nu_i^j$  under an affine transformation, we obtain

$$\sum_{i=1}^d \nu'^i_i = \sum_{i=1}^d \sum_{k=1}^d \sum_{\ell=1}^d \mathbf{A}_i^k (\mathbf{A}^{-1})_{\ell}^i \nu_k^{\ell} = c. \quad (1.39)$$

Thanks to the common index  $i$ , the matrices  $\mathbf{A}$  and  $\mathbf{A}^{-1}$  are multiplied as matrices, the result is the identity matrix and the contraction remains unchanged regardless of the transformation. Thanks to this property, affine invariants can be derived by means of a tensor contraction. The total contraction (i.e. contraction over all indices) of any tensor is an affine invariant.

### 1.6.5 Transformations of Tensor Fields

Let us consider a stress tensor field

$$\boldsymbol{\sigma}(\mathbf{x}) = \boldsymbol{\sigma}(x^1, x^2, x^3) \in \mathbb{R}^{3 \times 3}. \quad (1.40)$$

Similarly to vector fields, tensor fields are transformed by a total transformation.

Let  $\mathbf{A}$  and  $\mathbf{B}$  be  $3 \times 3$  regular matrices representing the inner and outer affine transformations, respectively

$$\mathbf{x}' = \sum_{(j,k)} (\mathbf{A}^{-1} \otimes \mathbf{x})_k^{ij} = \mathbf{A}^{-1} \mathbf{x} \quad (1.41)$$

and

$$\boldsymbol{\sigma}' = \mathbf{B}(\boldsymbol{\sigma}) = \sum_{(i,m)}_{(j,n)} (\mathbf{B} \otimes \mathbf{B} \otimes \boldsymbol{\sigma})_{ij}^{k\ell mn} = \mathbf{B}_i^k \mathbf{B}_j^{\ell} \boldsymbol{\sigma}^{ij}. \quad (1.42)$$

So, we have a total transformation

$$\boldsymbol{\sigma}'(\mathbf{x}') = \mathbf{B}(\boldsymbol{\sigma}(\mathbf{A}^{-1} \mathbf{x})). \quad (1.43)$$

### 1.6.6 Permutation Tensor

Most tensors in practice are purely contravariant and we cannot contract them directly. In these cases, we can use *permutation tensor*  $\varepsilon$ . In 2D, it takes the form

$$\varepsilon_{ij} = \begin{pmatrix} 0 & 1 \\ -1 & 0 \end{pmatrix}. \quad (1.44)$$

In 3D, it is an analogous  $3 \times 3 \times 3$  cube. The permutation tensor has six non-zero components at the positions where all three indices are different. If the index values are a cyclic shift of 123, the value is 1; if they are a cyclic shift of 321, the value is  $-1$ . In the remaining 21 positions, the value is 0. The permutation tensor can be used both as covariant  $\varepsilon_{i_1 \dots i_d}$  and as contravariant  $\varepsilon^{i_1 \dots i_d}$ . We can compute contractions of products of the covariant permutation tensors and contravariant tensors.

### 1.6.7 Moment Tensor

Geometric moments of a tensor field are defined as

$$m_{pqr}^{(ij)} = \int_{-\infty}^{\infty} \int_{-\infty}^{\infty} \int_{-\infty}^{\infty} x^p y^q z^r \sigma^{ij}(x, y, z) dx dy dz. \quad (1.45)$$

The moments of order  $o$  can be arranged to the *moment tensor*  ${}^o\mathbf{M}$ . For general tensors we have

$${}^o\mathbf{M}_{j_1 \dots j_m}^{k_1 \dots k_o i_1 \dots i_n} = \int_{\mathbb{R}^d} x^{k_1} \dots x^{k_o} \sigma_{j_1 \dots j_m}^{i_1 \dots i_n} (x^1 \dots x^d) d^d x, \quad (1.46)$$

where  $m$  is the covariant rank of the tensor field and  $n$  is its contravariant rank. For example, the moment tensor of Cauchy stress tensor is

$${}^o\mathbf{M}^{k_1 \dots k_o i j} = \int_{-\infty}^{\infty} \int_{-\infty}^{\infty} \int_{-\infty}^{\infty} x^{k_1} \dots x^{k_o} \sigma^{ij} (x^1, x^2, x^3) dx^1 dx^2 dx^3. \quad (1.47)$$

The components of the moment tensor equal the geometric moments

$${}^o\mathbf{M}_{j_1 \dots j_m}^{k_1 \dots k_o i_1 \dots i_n} = m_{p_1 \dots p_d(j_1 \dots j_m)}^{(i_1 \dots i_n)} \quad (1.48)$$

if and only if  $p_\ell$  of the indices  $k_1, \dots, k_o$  equals  $\ell$  for all  $\ell = 1, \dots, d$ .

The moment tensor of a tensor field has generally three types of indices: the covariant and contravariant indices of the original tensor field, and the contravariant indices from the integration over the coordinates (coordinate indices).

### 1.6.8 Construction of TFAMI

Now we can proceed to construct the *Tensor Field Affine Moment Invariants* (TFAMI). We can use the permutation tensors for the total contraction of a tensor product of moment tensors of a tensor field with both contravariant and covariant ranks. For

simplification, we limit ourselves only to contravariant tensor fields of the rank two. An example of such an invariant is

$$\begin{aligned} I &= \sum_{\substack{(i_1, i_2)(j_1, j_2) \\ (k_1, k_2)(\ell_1, \ell_2)(m_1, m_2) \\ (n_1, n_2)(o_1, o_2)(p_1, p_2)(q_1, q_2)}} {}^2\mathbf{M}^{i_1 j_1 k_1 \ell_1} \otimes {}^1\mathbf{M}^{m_1 n_1 o_1} \otimes {}^0\mathbf{M}^{p_1 q_1} \otimes \varepsilon_{i_2 k_2 n_2} \otimes \varepsilon_{j_2 m_2 p_2} \otimes \varepsilon_{\ell_2 o_2 q_2} \\ &= {}^2\mathbf{M}^{ijkl} {}^1\mathbf{M}^{mno} {}^0\mathbf{M}^{pq} \varepsilon_{ikn} \varepsilon_{jmp} \varepsilon_{\ell oq}. \end{aligned} \quad (1.49)$$

The invariant is computed as a total contraction of tensor product of moment tensors and permutation tensors, the invariance is reached as in Eq.(1.39). According to the Einstein notation in the last row, the sum symbols over all indices from 1 to  $d$  are omitted.

If we want to generate all the affine invariants of a tensor field, we need to generate all total contractions of the type Eq.(1.49), i.e. all tensor products of moment tensors and permutation tensors, where each index is used exactly twice (once in the moment tensor and once in the permutation tensor).

## 1.6.9 Experiments

### 1.6.9.1 Diffusion Tensor Imaging Data

An example of using tensors in medicine is a *Diffusion Tensor Imaging* (DTI). DTI is a modern MRI-based technique for an examination of tissues with internal anisotropic structure, such as neural axons of white matter in the brain and peripheral nerve fibres. It basically maps the diffusion of water molecules in each voxel by measuring their movement in several distinct directions. This measurement is accomplished via several diffusion-weighted acquisitions, each obtained with a different orientation of the diffusion sensitizing gradients. After obtaining a complete set of such measurements (six diffusion-encoding gradient directions are the minimum needed to calculate the diffusion tensor; usually 30, 64 or more gradient directions are used), a symmetric second-rank  $3 \times 3$  tensor is calculated in each voxel. This tensor image is an extremely useful modality, because it offers a possibility to detect a subtle pathology in the brain, to track neural tracts through the brain (this process is called tractography), to examine the integrity of peripheral nerves, and to diagnose of many neurological diseases [2, 30, 7].

In this experiments, we used real DTI scans of a human brain. The device used for an examination was a 3T Siemens TrioTim MR scanner using spin-echo echo-planar imaging (SE EPI) sequence. The acquisition parameters were the following: repetition time (TR) of 8300 ms, echo time (TE) of 84 ms, voxel size of  $2 \times 2 \times 2$  mm, 68 axial slices, two averages, field of view (FOV) of 256 mm, number of diffusion directions 30, two  $b$ -values: 0, and  $900 \text{ s/mm}^2$ . The data were acquired and provided by the Institute for Clinical and Experimental Medicine (IKEM) in Prague, Czech Republic.

The volumes of diffusion data were stacked together (as described in [15]) to produce 3D volume of a  $3 \times 3$  symmetric diffusion tensor. Three sample slices are shown in Fig.(1.9). Since the tensor field cannot be visualized entirely, we show fractional anisotropy with color-encoded prevailing direction.

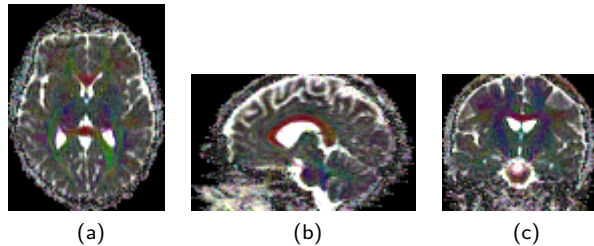


Figure 1.9: The original diffusion tensor field. Slices in (a) axial, (b) sagittal and (c) coronal plane. The colors show the prevailing diffusion direction (blue: superior-inferior, green: anterior-posterior, and red: left-right).

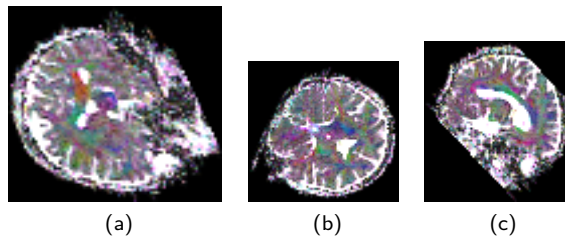


Figure 1.10: Sample affine-transformed tensor field. Slices in (a) x-y plane, (b) x-z plane, (c) y-z plane.

### 1.6.9.2 Invariance Verification

We generated ten random affine transformations of our diffusion tensor field (see Fig.(1.10) for one of them) and calculated 197 invariants for every transformed data. The values of four selected invariants are shown in Fig.(1.11), the behavior of the others is essentially the same. The labels 1 – 10 on the horizontal axis denote the individual affine transformations, while 0 stands for the original field.

The mean relative error over all invariants and all affine transformations is 1.04% and is caused almost solely by resampling errors when the field was transformed. To prove that, we calculated the moments of the transformed field directly from the original field (we could do that thanks to the knowledge of the transformation parameters) without any resampling and we substituted these moments into the invariants. The mean relative error then decreased to  $1.26 \cdot 10^{-12}\%$  which shows that our descriptors are actually invariant.

### 1.6.9.3 Template Matching

We randomly selected 10 spherical non-overlapping templates with the diameter 15 voxels (see Fig.(1.12) for an example). Then we deformed the entire tensor field by an affine transformation and tried to localize the templates in the deformed field. We repeated this experiment twice.

The last experiment demonstrates the added value, provided by the tensor invariants, over “traditional” scalar image invariants. We repeated the same template matching

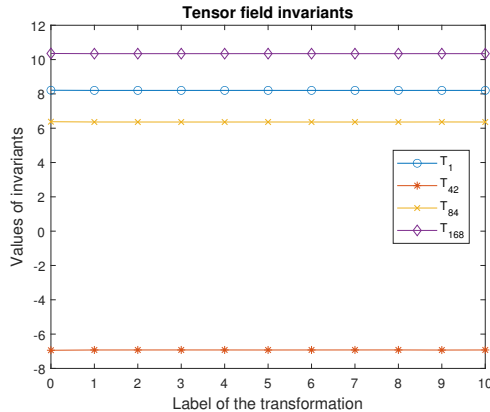


Figure 1.11: The values of four selected TFAMIs over ten random affine transformations.

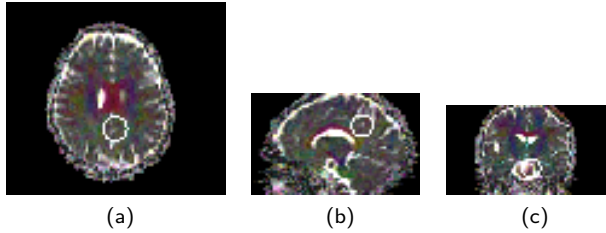


Figure 1.12: A sample spherical template extracted from the original tensor field. Slices in (a) axial, (b) sagittal and (c) coronal plane.

but used only the fractional anisotropy data, calculated from the tensor field, that can be viewed as a monochromatic 3D image. Instead of tensor invariants, we applied 3D affine moment invariants for scalar images [31, 11] of the same order. We set the other parameters the same as in Fig.(1.13). The localization errors are shown in Fig.(1.14).

We searched the tensor field voxel by voxel, computed 205 TFAMIs from the 2nd to the 6th order, and evaluated the similarity between the template and the field patch by  $\ell_2$ -norm in the space of the TFAMIs. The patch with the minimum  $\ell_2$ -distance from the template was selected as the match.

Since the ground-truth positions are known in this simulated experiment, we measured the localization errors (Euclidean distance in voxels between the detected match and the ground truth). The sorted errors can be seen in Fig.(1.13). We can see that only one localization error (out of 20) is greater than 3 voxels, which is an acceptable accuracy.

The last experiment demonstrates the added value, provided by the tensor invariants, over “traditional” scalar image invariants. We repeated the same template matching but used only the fractional anisotropy data, calculated from the tensor field, that can be viewed as a monochromatic 3D image. Instead of tensor invariants, we applied 3D

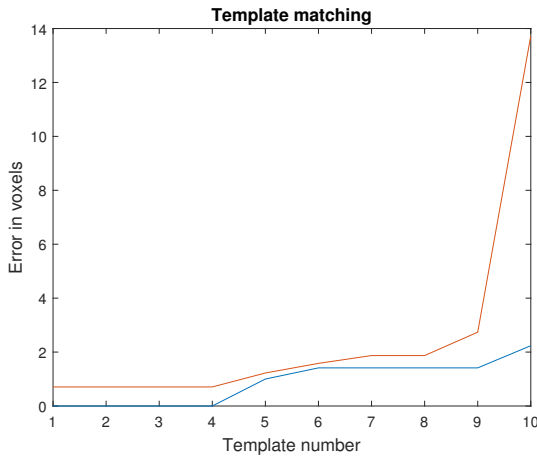


Figure 1.13: Localization errors in the template matching experiment -- first run (red curve) and second run (blue curve) for the template diameter 15 voxels. Tensor field invariants of order from 2 to 6 were used. The templates are sorted according to their localization errors.

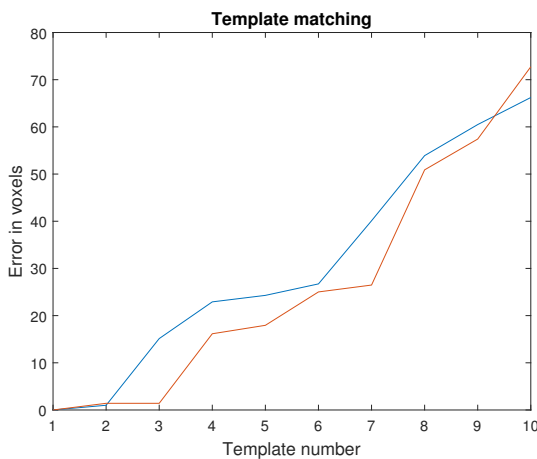


Figure 1.14: Localization errors in the template matching experiment – first run (red curve) and second run (blue curve) for the template diameter 15 voxels. Scalar 3D affine invariants of order from 2 to 6 were used on fractional anisotropy image.

affine moment invariants for scalar images [31, 11] of the same order. We set the other parameters the same as in Fig.(1.13). The localization errors are shown in Fig.(1.14).

In all runs, the accuracy was significantly worse than in the case of tensor field. There are basically two reasons for such a performance drop. Scalar value of fractional anisotropy does not capture directional information; two image patches may look similar even if they differ substantially from one another in the original tensor field. The second reason is that for the given moment order, we have much more tensor invariants than scalar invariants, that results in different recognition abilities.

## 1.7 Conclusions

In this chapter, we reviewed invariants of vector and tensor fields with respect to total affine transformation. We showed that the behavior of the fields under a total affine transformation is significantly different from that of scalar and color images under standard affine transformation and the traditional techniques cannot be used. We demonstrated the performance of the invariants in various template matching experiments.

## Acknowledgement

This work has been supported by the Czech Science Foundation (Grant No. GA18-07247S), by the Ministry of Health of the Czech Republic – DRO (IKEM, IN 00023001), and by the *Praemium Academiae*. The authors thank Prof. Mario Hlawitschka and Dr. Roxana Bujack for providing the Karman vortex street data, the NOAA ESRL Physical Sciences Division, Boulder, Colorado, for providing the satellite wind maps, and IKEM for providing the DTI data.

## References

- [1] Yaser S. Abu-Mostafa and Demetri Psaltis. Recognitive aspects of moment invariants. *IEEE Transactions on Pattern Analysis and Machine Intelligence*, 6(6):698–706, 1984.
- [2] Andrew L. Alexander, Jee Eun Lee, Mariana Lazar, and Aaron S. Field. Diffusion tensor imaging of the brain. *Neurotherapeutics*, 4(1):316–329, 2007.
- [3] Roxana Bujack and Jan Flusser. Flexible basis of rotation moment invariants. In Václav Skala, editor, *International Conferences in Central Europe on Computer Graphics, Visualization and Computer Vision WSCG'17*, pages 11–20, 2017.
- [4] Roxana Bujack and Hans Hagen. Moment Invariants for Multi-Dimensional Data. In Evren Ozerslan, Thomas Schultz, and Ingrid Hotz, editors, *Modelling, Analysis, and Visualization of Anisotropy*, Mathematica and Visualization, Basel, 2017. Springer.
- [5] Roxana Bujack, Mario Hlawitschka, Gerik Scheuermann, and Eckhard Hitzer. Customized TRS invariants for 2D vector fields via moment normalization. *Pattern Recognition Letters*, 46(1):46–59, 2014.

- [6] Roxana Bujack, Ingrid Hotz, Gerik Scheuermann, and Eckhard Hitzer. Moment invariants for 2D flow fields using normalization. In *Pacific Visualization Symposium, PacificVis'14*, pages 41–48. IEEE, March 2014.
- [7] Marius de Groot, Lotte G. M. Cremers, M. Arfan Ikram, Albert Hofman, Gabriel P. Krestin, Aad van der Lugt, Wiro J. Niessen, and Meike W. Vernooij. White matter degeneration with aging: Longitudinal diffusion MR imaging analysis. *Radiology*, 279(2):532–541, 2015.
- [8] Jan Flusser. On the independence of rotation moment invariants. *Pattern Recognition*, 33(9):1405–1410, 2000.
- [9] Jan Flusser. On the inverse problem of rotation moment invariants. *Pattern Recognition*, 35(12):3015–3017, 2002.
- [10] Jan Flusser and Tomáš Suk. Pattern recognition by affine moment invariants. *Pattern Recognition*, 26(1):167–174, 1993.
- [11] Jan Flusser, Tomáš Suk, and Barbara Zitová. *2D and 3D Image Analysis by Moments*. Wiley, Chichester, U.K., 2016.
- [12] Ming Gong, You Hao, Hanlin Mo, and Hua Li. Naturally combined shape-color moment invariants under affine transformations. *Computer Vision and Image Understanding*, 162:46–56, 2017.
- [13] Mark S. Hickman. Geometric moments and their invariants. *Journal of Mathematical Imaging and Vision*, 44(3):223–235, 2012.
- [14] Eugenia Kalnay, Masao Kanamitsu, Robert Kistler, William Collins, Dennis Deaven, Lev Gandin, Mark Iredell, Suranjana Saha, Glenn White, John Woollen, et al. The NCEP/NCAR 40-year reanalysis project. *Bulletin of the American Meteorological Society*, 77(3):437–472, 1996.
- [15] Peter B Kingsley. Introduction to diffusion tensor imaging mathematics: Part i-iii. *Concepts in Magnetic Resonance Part A*, 28(2):101–179, 2006.
- [16] Jitka Kostková, Tomáš Suk, and Jan Flusser. Affine moment invariants of vector fields. In *2018 25th IEEE International Conference on Image Processing (ICIP)*, pages 1338–1342. IEEE, 2018.
- [17] Jitka Kostková, Tomáš Suk, and Jan Flusser. Affine invariants of vector fields. *IEEE Transactions on Pattern Analysis and Machine Intelligence*, (10.1109/TPAMI.2019.2951664), 2019.
- [18] Max Langbein and Hans Hagen. A generalization of moment invariants on 2D vector fields to tensor fields of arbitrary order and dimension. In *Proceedings of 5th International Symposium Advances in Visual Computing, ISVC'09, Part II*, volume 5876 of *Lecture Notes in Computer Science*, pages 1151–1160. Springer, 2009.
- [19] Manhua Liu and Pew-Thian Yap. Invariant representation of orientation fields for fingerprint indexing. *Pattern Recognition*, 45(7):2532–2542, 2012.
- [20] Wei Liu and Eraldo Ribeiro. Detecting singular patterns in 2-D vector fields using weighted Laurent polynomial. *Pattern Recognition*, 45(11):3912–3925, 2012.
- [21] Florica Mindru, Tinne Tuytelaars, Luc Van Gool, and Theo Moons. Moment invariants for recognition under changing viewpoint and illumination. *Computer Vision and Image Understanding*, 94(1–3):3–27, 2004.
- [22] Thomas H. Reiss. The revised fundamental theorem of moment invariants. *IEEE Transactions on Pattern Analysis and Machine Intelligence*, 13(8):830–834, 1991.

- [23] Thomas H. Reiss. *Recognizing Planar Objects Using Invariant Image Features*, volume 676 of *LNCS*. Springer, Berlin, Germany, 1993.
- [24] Michael Schlemmer, Manuel Heringer, Florian Morr, Ingrid Hotz, Martin-Hering Bertram, Christoph Garth, Wolfgang Kollmann, Bernd Hamann, and Hans Hagen. Moment invariants for the analysis of 2D flow fields. *IEEE Transactions on Visualization and Computer Graphics*, 13(6):1743–1750, 2007.
- [25] Tomáš Suk and Jan Flusser. Graph method for generating affine moment invariants. In *Proceedings of the 17th International Conference on Pattern Recognition ICPR'04*, pages 192–195. IEEE Computer Society, 2004.
- [26] Tomáš Suk and Jan Flusser. Affine moment invariants of color images. In Xiaoyi Jiang and Nikolai Petkov, editors, *Computer Analysis of Images and Patterns CAIP'09*, volume LNCS 5702, pages 334–341. Springer, September 2009.
- [27] Tomáš Suk and Jan Flusser. Affine moment invariants generated by graph method. *Pattern Recognition*, 44(9):2047–2056, 2011.
- [28] M. R. Teague. Image analysis via the general theory of moments. *Journal of the Optical Society of America*, 70(8):920–930, 1980.
- [29] Åke Wallin and Olaf Kübler. Complete sets of complex Zernike moment invariants and the role of the pseudoinvariants. *IEEE Transactions on Pattern Analysis and Machine Intelligence*, 17(11):1106–1110, 1995.
- [30] Claudia Angela Michela Gandini Wheeler-Kingshott, Simon J. Hickman, Geoffrey J. M. Parker, Olga Ciccarelli, Mark R. Symms, David H. Miller, and Gareth John Barker. Investigating cervical spinal cord structure using axial diffusion tensor imaging. *NeuroImage*, 16(1):93–102, 2002.
- [31] Dong Xu and Hua Li. 3-D affine moment invariants generated by geometric primitives. In *Proceedings of the 18th International Conference on Pattern Recognition ICPR'06*, pages 544–547, Los Alamitos, California, USA, 2006. IEEE Computer Society.
- [32] Bo Yang and Mo Dai. Image analysis by Gaussian–Hermite moments. *Signal Processing*, 91(10):2290–2303, 2011.
- [33] Bo Yang, Jan Flusser, and Jaroslav Kautsky. Rotation of 2D orthogonal polynomials. *Pattern Recognition Letters*, 102(1):44–49, 2018.
- [34] Bo Yang, Jan Flusser, and Tomáš Suk. Design of high-order rotation invariants from Gaussian–Hermite moments. *Signal Processing*, 113(1):61–67, 2015.
- [35] Bo Yang, Jitka Kostková, Jan Flusser, Tomáš Suk, and Roxana Bujack. Rotation invariants of vector fields from orthogonal moments. *Pattern Recognition*, 74:110–121, 2018.
- [36] Bo Yang, Jitka Kostková, Tomáš Suk, Jan Flusser, and Roxana Bujack. Recognition of patterns in vector fields by Gaussian–Hermite invariants. In Jiebo Luo, Wenjun Zeng, and Yu-Jin Zhang, editors, *International Conference on Image Processing ICIP'17*, pages 2350–2363. IEEE, 2017.
- [37] Bo Yang, Gengxiang Li, Hui long Zhang, and Mo Dai. Rotation and translation invariants of Gaussian–Hermite moments. *Pattern Recognition Letters*, 32(2):1283–1298, 2011.
- [38] Frits Zernike. Beugungstheorie des Schneidenverfahrens und seiner verbesserten Form, der Phasenkontrastmethode. *Physica*, 1(7):689–704, 1934. (in German).